# Scale and orientation signatures of soil structure in thin sections: a hierarchical descriptor tensor applied to greenhouse soils under conventional, pollution-free and organic management

Ştefan Ţălu

The Directorate of Research, Development and Innovation Management (DMCDI), The Technical University of Cluj-Napoca, Cluj-Napoca, Romania. Corresponding author: Ş. Ţălu, stefan.talu@auto.utcluj.ro

https://doi.org/10.67784/0099

**Abstract**. Soil structure is a key indicator of soil health, and thin sections show it directly, but its image analysis usually depends on segmenting pores and reports single-scale, orientation-averaged quantities. This study applies a hierarchical descriptor tensor, indexed by descriptor channel, Gaussian scale, orientation and region of interest (ROI), to nine published plane-polarized-light micrographs of a greenhouse clay-loam soil after ten years of conventional (CPP), pollution-free (PFP) and organic (OPP) management, at depths of 0–10, 10–20 and 20–40 cm. Ten channels were evaluated at six scales (1.7–55 µm) and four orientations for one and four ROIs, with isotropic surrogates and a block bootstrap as references. One image, dominated by a single plant residue, was excluded. The readouts that separated the management systems were the scale readouts, not anisotropy. At 0–10 and 20–40 cm the mean correlation length ranked CPP < PFP < OPP (0–10 cm: 10.9, 25.5 and 31.3 µm), as did the characteristic scale (3.8, 13.7 and 18.7 µm), gradient kurtosis and autocorrelation; at 10–20 cm, where the OPP image was excluded, CPP ranked below PFP for all four readouts. Across the eight images, the correlation length agreed with the mean pore diameter reported for the same plots (Spearman $\rho = 0.86$, $n = 8$; $P = 0.007$ by the t approximation, 0.011 by exact permutation). At 3.4 µm, all images were only weakly anisotropic ($A = 0.034–0.214$); the anisotropy index rose with bulk density ($\rho = 0.80$) and with depth. The texture axis matched the visible planar voids, cracks and channels: vertical planar voids at 93°, a diagonal crack at 36°, and a residue channel at 22°. At the aggregate scale (27.6 µm), the crumb microstructure of the organic surface soil did not exceed the isotropic floor ($A = 0.066$, surrogate 95th percentile 0.106). Clustering of the 32 regional tensors grouped blocky and crumb microstructures rather than management systems. The tensor therefore gives interpretable, physically scaled and exploratory readings of soil structure without segmentation. Because each management–depth combination is represented by a single published field, these results are not a test of management effects.

**Keywords:** soil micromorphology, soil structure, thin section, texture analysis, descriptor tensor, anisotropy, correlation length, organic farming, soil compaction, greenhouse soil.

**Introduction**. Soil structure, the arrangement of solid particles and of the pores between them, controls water retention and drainage, aeration, root growth and the habitat of soil organisms, and is therefore among the most informative indicators of soil functioning and soil health (Bronick & Lal, 2005; Rabot et al., 2018). It responds directly to management: compaction by traffic and tillage reduces macroporosity and produces dense, platy or massive fabrics, whereas inputs of organic matter favour the formation and stabilisation of aggregates and of biological pores (Pagliai et al., 2004; Hamza & Anderson, 2005). In intensively cultivated greenhouse soils of the North China Plain, long-term mineral fertilisation has been associated with structural degradation, while organic management increased organic matter, aggregation and porosity (Liu et al., 2019).

Soil micromorphology describes structure directly in thin sections of undisturbed, resin-impregnated soil (Stoops, 2021; Verrecchia & Trombino, 2021). Description remains largely qualitative (microstructure type, degree of separation of aggregates, void types), and quantification usually proceeds by segmenting the pore space and measuring

the size, shape and orientation of the resulting objects (Ringrose-Voase, 1991; Pagliai et al., 2004), or by scaling descriptors such as fractal dimensions (Perfect & Kay, 1995). Segmentation-based measurements depend on the threshold and on the separation of touching pores, and most summary indices are reported at a single scale and without a direction. Texture analysis offers a complementary route that describes how image intensity varies in space without segmentation (Haralick et al., 1973; Ţălu, 2012), but texture values depend jointly on the scale at which they are observed, the direction in which they are probed and the region over which they are summarized (Depeursinge, 2017), and on computational settings that are often under-reported (Zwanenburg et al., 2020; Traverso et al., 2018).

A hierarchical descriptor tensor that keeps scale, orientation and region as separate indices of every measurement was formulated and applied to histological sections of human and fish skeletal muscle (Ţălu, 2027a), within a broader multidimensional framework for quantitative image-based assessment (Ţălu, 2026a), and has since been used for guppy, porcine and rabbit muscle (Ţălu, 2026b, 2027b, 2027c). Soil thin sections are a natural further test of the framework, because the structures that distinguish healthy from degraded soil differ precisely in scale (the size of aggregates and pores), in orientation (planar voids and plates produced by compaction, channels produced by roots and fauna) and in regional heterogeneity. They also differ from tissue images in one important respect: the intensity is dominated by two phases, the solid matrix and the resin-filled pores. Building on micromorphological surface and texture characterization approaches (Ţălu, 2015), the present study asks three questions. (i) Which readouts of the tensor – anisotropy, texture axis, characteristic scale or spatial correlation – differ between soils that have been under conventional, pollution-free and organic management for ten years? (ii) Do the texture axes correspond to structures that are visible in the micrographs? (iii) Do the tensor readouts agree with independent micromorphometric and physical measurements made on the same plots? The analysis uses published, openly licensed micrographs (Liu et al., 2019), so the aim is to establish whether the tensor gives interpretable and internally consistent readings of soil structure, not to estimate management effects.

## Theoretical Framework

***Hierarchical descriptor tensor.*** Let $f(\mathbf{x})$, $\mathbf{x} \in \Omega \subset \mathbb{R}^2$, be the luminance of a thin-section micrograph, standardized to zero mean and unit variance. Structure at scale $s$ is probed through the Gaussian scale-space $G_s = g_s * f$, where $g_s$ is the isotropic Gaussian of standard deviation $s$ (Lindeberg, 1998). Directional sensitivity is introduced by the unit vector $\mathbf{u}_\theta = (\cos\theta, \sin\theta)^\mathrm{T}$ (angle measured counter-clockwise from the image rows, with the $y$ axis pointing upward) and the steerable directional derivatives (Freeman & Adelson, 1991)

$$\partial_\theta G_s = \mathbf{u}_\theta \cdot \nabla G_s, \qquad \partial_\theta^2 G_s = \mathbf{u}_\theta^\mathrm{T} \nabla\nabla^\mathrm{T} G_s \, \mathbf{u}_\theta \qquad (1)$$

For a set of regions $\Omega_1, \ldots, \Omega_R \subseteq \Omega$, each channel $m$ maps a local response to a regional summary $D_m(s, \theta, \Omega_r)$. Sampling $K$ scales and $L$ orientations, the measurements form the fourth-order array

$$\mathfrak{D} \in \mathbb{R}^{M \times K \times L \times R}, \qquad \mathfrak{D}_{mklr} = D_m(s_k, \theta_l, \Omega_r) \qquad (2)$$

The indices are kept separate on purpose: a value is meaningful only with its scale, orientation and region. In the reference configuration there are $M = 10$ channels (Table 1), $K = 4$ scales ($s = 1{,}2{,}4{,}8$ px), $L = 4$ orientations ($\theta = 0, \pi/4, \pi/2, 3\pi/4$) and $R = 1$ or $R = 4$ regions, giving 160 or 640 entries per image. Filters are applied to the whole image with reflective boundaries and only the aggregation is restricted to $\Omega_r$, so region borders do not create artificial edges.

Table 1

Channels of the descriptor tensor.

All channels are evaluated for every $(s_k, \theta_l, \Omega_r)$; $\langle\cdot\rangle_r$ is the mean over $\Omega_r$.

| *Channel* | *Definition* | *Type* |
|---|---|---|
| D1 | $\langle \lvert \partial_\theta G_s \rvert \rangle_r$ | Gradient amplitude |
| D2 | $\langle (\partial_\theta G_s)^2 \rangle_r$ (Directional energy) | Gradient energy |
| D3 | Kurtosis of $\partial_\theta G_s$ over $\Omega_r$ | Gradient distribution Shape |
| D4 | Shannon entropy of $\partial_\theta G_s$ (32 bins over ± 4 SD, bits) | Gradient distribution shape |
| D5 | $\langle \lvert \partial_\theta^2 G_s \rvert \rangle_r$ | Second-derivative amplitude |
| D6–D9 | GLCM contrast, homogeneity, energy, correlation of $G_s$ (16 levels; symmetric offsets $\pm d$, $d = s$ along $\theta$, rounded to integer pixels) | Co-occurrence (Haralick et al., 1973) |
| D10 | Normalized autocorrelation of $G_s$ at lag $2s$ along $\pm\theta$ | Spatial correlation |

***Directional energy as a quadratic form.*** Define the regional second-moment (structure) matrix (Bigün & Granlund, 1987)

$$\mathbf{J}_{s,r} = \langle \nabla G_s \, \nabla G_s^{\mathrm{T}} \rangle_r = \begin{pmatrix} J_{xx} & J_{xy} \\ J_{xy} & J_{yy} \end{pmatrix} \qquad (3)$$

**Proposition 1.** For every scale and region, $D_2(s, \theta, \Omega_r) = \mathbf{u}_\theta^{\mathrm{T}} \mathbf{J}_{s,r} \mathbf{u}_\theta$, that is

$$D_2(\theta) = 1/2\,(\lambda_+ + \lambda_-) + 1/2\,(\lambda_+ - \lambda_-)\cos 2(\theta - \varphi) \qquad (4)$$

where $\lambda_+ \geq \lambda_-$ are the eigenvalues of $\mathbf{J}_{s,r}$ and $\varphi$ the direction of its leading eigenvector. With the configured orientations, $J_{xx} = D_2(0)$, $J_{yy} = D_2(\pi/2)$ and $J_{xy} = 1/2\,[D_2(\pi/4) - D_2(3\pi/4)]$.

*Proof.* $\partial_\theta G_s$ is linear in $\mathbf{u}_\theta$, so $(\partial_\theta G_s)^2 = \mathbf{u}_\theta^{\mathrm{T}} \nabla G_s \nabla G_s^{\mathrm{T}} \mathbf{u}_\theta$; averaging over $\Omega_r$ gives the quadratic form, and the spectral decomposition of $\mathbf{J}_{s,r}$ gives (4). Evaluating (4) at $0, \pi/2, \pi/4, 3\pi/4$ gives the three entries. ▫

Three consequences are used throughout. First, the anisotropy index and the texture axis

$$A = \frac{\max_\theta D_2 - \min_\theta D_2}{\max_\theta D_2 + \min_\theta D_2} = \frac{\lambda_+ - \lambda_-}{\lambda_+ + \lambda_-}, \qquad \psi = \varphi + \frac{\pi}{2} \ (\mathrm{mod}\ \pi) \qquad (5)$$

are determined exactly by the four tensor entries, although the true axis need not coincide with a configured orientation. Reading $A$ directly from the four sampled values gives a lower bound $A_4$ with $A/\sqrt{2} \leq A_4 \leq A$; for this reason $A$ and $\psi$ are computed from (5). Second, the four entries satisfy $D_2(0) + D_2(\pi/2) = D_2(\pi/4) + D_2(3\pi/4)$, which is a computational check. Third, with the doubled-angle field $z_s = \left(\partial_x G_s + i\, \partial_y G_s\right)^2$, $A = |\langle z_s \rangle_r| / \langle |z_s| \rangle_r$: the anisotropy index is the energy-weighted mean resultant length of the doubled gradient directions (Mardia & Jupp, 2000). In a soil thin section, gradients are perpendicular to the boundaries between the solid phase and the resin-filled pores, so $\psi$ is the dominant direction of these boundaries (for example of planar voids, cracks and elongated channels) in the image plane, and $A$ measures how consistently they share it.

The same quantities define a local field. Replacing the regional mean in (3) by a Gaussian-weighted local mean of width $\rho$ gives the structure-tensor field $\mathbf{J}_{s,\rho}(\mathbf{x})$, whose local axis and coherence $\kappa = (\lambda_+ - \lambda_-)/(\lambda_+ + \lambda_-)$ describe how orientation varies across the section (Bigün & Granlund, 1987). The regional $A$ and the mean local $\kappa$ are not the same quantity: $A$ is high only if local orientations agree across the region.

***Regional aggregation: the pooling inequality.*** The ROI index of the tensor allows a section to be summarized either as one region or as several. For mean-type channels (D1, D2, D5 and the elements of $\mathbf{J}$), the summary of a union of equal-area regions is the mean of the regional summaries. The anisotropy index is not additive in this way.

**Proposition 2 (pooling inequality).** Let $\Omega = \bigcup_{r=1}^{R} \Omega_r$ be a partition into regions of equal area, with regional anisotropy $A_r$ and regional energy $E_r = \mathrm{tr}\mathbf{J}_{s,r}$. Then

$$A(\Omega) \leq \frac{\sum_r E_r A_r}{\sum_r E_r} \qquad (6)$$

with equality if and only if all regions with $A_r > 0$ have the same texture axis.

*Proof.* With equal areas, $\langle z_s\rangle_\Omega = R^{-1}\sum_r \langle z_s\rangle_r$ and $\langle |z_s|\rangle_\Omega = R^{-1}\sum_r E_r$. Since $|\langle z_s\rangle_r| = A_r E_r$, the triangle inequality gives $A(\Omega) = |\sum_r \langle z_s\rangle_r| / \sum_r E_r \le \sum_r A_r E_r / \sum_r E_r$, with equality if and only if the complex numbers $\langle z_s\rangle_r$ have the same argument, i.e. the same $\psi$. ▫

Proposition 2 makes precise a point that is often stated qualitatively: aggregating a heterogeneous region attenuates directional organization, and the attenuation is a direct measure of the disagreement between regional axes. The ratio $A(\Omega)/\sum_r E_r A_r / \sum_r E_r$ is therefore a scale-specific index of directional coherence across the section.

***Scale: variance loss and characteristic scale***. Because the Gaussian scale-space satisfies the diffusion equation $\partial_t G = \Delta G$ with $t = s^2/2$, the variance $V(s) = \langle G_s^2\rangle$ decreases with scale at a rate given by the total gradient energy. Under periodic or no-flux boundaries,

$$s^2 \mathrm{tr}\mathbf{J}_s = -\frac{1}{2}\frac{dV}{d\ln s} \qquad (7)$$

so the scale-normalized energy $s^2\mathrm{tr}\mathbf{J}_s$ (Lindeberg, 1998) is the rate at which image variance is lost per unit of log-scale. Its maximum $s^*$ marks the scale at which the image loses most variance, i.e. the dominant width of its intensity transitions. For a Gaussian random field $s^*$ equals the correlation scale; for images with sharp phase boundaries, such as thin sections, no such identity holds, and $s^*$ is read as a descriptor-specific indicator of the width of the dominant edges. An image whose variance is lost evenly over a range of scales shows a plateau rather than a peak.

***Spatial correlation: autocovariance, correlation length and co-occurrence***. Let $C_s(\mathbf{h}) = \langle G_s(\mathbf{x})G_s(\mathbf{x}+\mathbf{h})\rangle$ be the autocovariance of the smoothed image and $\gamma_s(\mathbf{h}) = C_s(\mathbf{0}) - C_s(\mathbf{h})$ its semivariogram. Then

$$\mathbf{J}_s = -\nabla\nabla^{\mathrm{T}} C_s(\mathbf{0}), \qquad D_2(s,\theta) = \lim_{h\to 0}\frac{2\gamma_s(h\mathbf{u}_\theta)}{h^2} \qquad (8)$$

so $D_2$ is the curvature of the autocovariance at the origin along $\theta$: high directional energy corresponds to a rapid loss of correlation in that direction. At finite lags this motivates the directional correlation length $\xi(\theta)$, the lag at which the normalized autocorrelation falls to $1/e$ along $\theta$; $\xi$ is expected to be shortest where $D_2$ is largest, but because it is measured at finite lag it weights coarser structure than $D_2$ at small $s$. The co-occurrence channels have the same variogram structure. For the symmetric co-occurrence matrix of the quantized image $Q$ at offset $\mathbf{d}$, the two marginals are equal, so contrast and correlation satisfy the identity

$$D_6 = 2\gamma_Q(\mathbf{d}), \qquad D_9 = 1 - \frac{\gamma_Q(\mathbf{d})}{\sigma_Q^2}, \qquad D_6 = 2\sigma_Q^2(1 - D_9) \qquad (9)$$

where $\sigma_Q^2$ is the variance of $Q$ over the pairs anchored in the region. D6 and D9 therefore carry the same information *only if* $\sigma_Q^2$ is constant across the entries compared; when $\sigma_Q^2$ varies with scale and region, as it does in real images, their rank correlation weakens even though each entry obeys (9) exactly.

***Reference for isotropy and uncertainty***. A real image has no replicate realizations and no ground truth. Two constructions provide the missing references. (i) *Isotropic surrogates*: for each image, surrogate fields are generated from the radially averaged Fourier amplitude of the image with uniformly random phases (Theiler et al., 1992). They have no preferred direction but the same radial spectrum, hence the same finite-sample floor of $A$, which depends on ROI size and correlation scale; an observed $A$ is compared with the 95th percentile of $A$ over the surrogates. (ii) *Block bootstrap*: each ROI is divided into blocks that are resampled with replacement (Künsch, 1989), and percentile intervals of $A$ and $\psi$ are reported. Surrogates test departure from an isotropic spectrum; they are Gaussian and do not reproduce the non-Gaussian intensity distribution of thin sections, in which the solid phase and the resin-filled pores form two distinct populations.

**Material and Method.** ***Soils and test images***. The images come from a ten-year greenhouse experiment (2003–2012) at the Quzhou Agriculture and Ecology Experimental Station of China Agricultural University (Hebei, North China Plain) on a clay-loam salinized fluvo-aquic soil (sand 22 %, silt 59 %, clay 19 %) under a tomato–cucumber rotation (Liu et al., 2019). Three planting patterns were compared: conventional planting (CPP) with mineral fertilisers and chemical plant protection; pollution-free planting (PFP) with 70 % organic and 30 % mineral fertiliser; and organic planting (OPP) with certified organic fertilisers only, and physical and biological pest control. Undisturbed cores were taken at 0–10, 10–20 and 20–40 cm in September 2013, impregnated and cut into 30-µm thin sections, which were photographed in plane-polarized light at 50× magnification (Liu et al., 2019). Figure 1 of that article shows one representative field for each pattern and depth (panels a–i), and these nine fields are the test images of the present study (Figure 1). Table 2 lists the microstructure reported for each field by the original authors. In the same study, organic management gave the lowest bulk density, the highest organic matter content and the highest proportion of water-stable macroaggregates at every depth, with PFP intermediate; in the 0–10 cm layer, bulk density was 1.33, 1.28 and 1.17 g $cm^{-3}$, and organic matter 26.8, 40.4 and 54.8 g $kg^{-1}$, for CPP, PFP and OPP (Liu et al., 2019).

***Image sources and permission to reproduce***. Liu et al. (2019) is an open-access article in *Scientific Reports* distributed under the Creative Commons Attribution 4.0 International licence (CC BY 4.0), which permits reuse, adaptation and redistribution in any medium provided that the original work is properly cited and changes are indicated. The nine panels of its Figure 1 were cropped from the published raster; their printed captions were removed; and ROI outlines and a calibrated scale bar were added (Figure 1). Pixel values were not otherwise modified. All other figures are new analyses produced by the author.

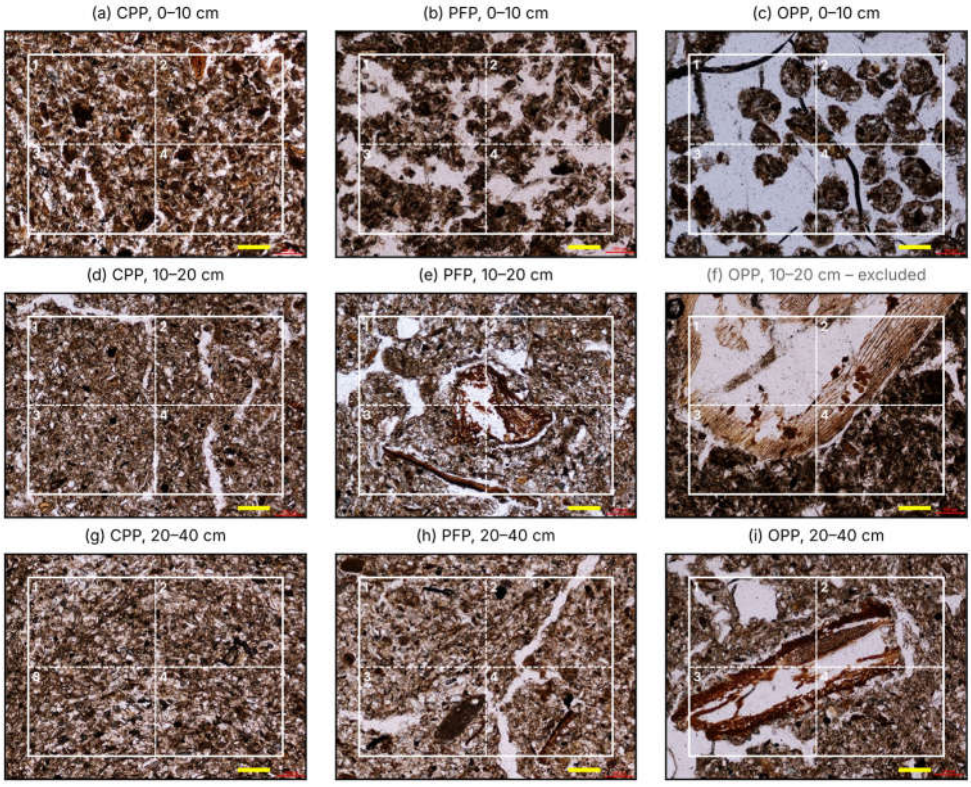


Figure 1. Test images and ROI layout. Plane-polarized-light micrographs of thin sections of a greenhouse clay-loam soil after ten years of conventional (CPP), pollution-free (PFP) and organic (OPP) planting, at 0–10, 10–20 and 20–40 cm (images a–i). Solid white rectangle: ROI = 1 (48-px margin removed); dashed: the four ROIs of the R = 4 configuration (1, upper left; 2, upper right; 3, lower left; 4, lower right). Yellow bar: 100 µm (58 px). Image f was excluded from the analysis (see text). Panels cropped from Figure 1 of Liu et al. (2019), © 2019 The Author(s), reproduced under the CC BY 4.0 licence; changes: original panel captions removed, ROI outlines and scale bar added.

Table 2

Test images (Figure 1 of Liu et al., 2019) and analysis geometry. Microstructure as described by the original authors. Skewness and kurtosis of the z-scored luminance f in ROI = 1 (Gaussian: 0 and 3)

| *Image* | *Pattern* | *Depth (cm)* | *Microstructure (Liu et al., 2019)* | *Raster (px)* | *Skewness / kurtosis* |
|---|---|---|---|---|---|
| a | CPP | 0–10 | moderately separated (angular) blocky | 622 × 466 | 0.66 / 2.48 |
| b | PFP | 0–10 | moderately separated crumb | 621 × 466 | 0.22 / 1.56 |
| c | OPP | 0–10 | highly developed crumb | 622 × 466 | -0.15 / 1.36 |
| d | CPP | 10–20 | mildly separated blocky | 622 × 466 | 0.66 / 2.69 |
| e | PFP | 10–20 | moderately separated blocky and crumb | 621 × 466 | 0.43 / 2.05 |
| f* | OPP | 10–20 | decomposed organic matter, fauna excrement | 622 × 466 | -0.00 / 1.47 |
| g | CPP | 20–40 | dense angular blocky | 622 × 466 | 0.47 / 2.31 |
| h | PFP | 20–40 | mildly separated angular blocky, planar voids | 621 × 466 | 0.26 / 2.00 |
| i | OPP | 20–40 | channels formed by decomposing residues | 622 × 466 | 0.33 / 1.73 |

* Excluded from comparisons. Pixel size 1.72 µm (100 µm = 58 px); ROI = 1: 526 × 370 px (525 × 370 px for b, e, h) = 0.90 × 0.64 mm; ROI = 4 quadrants: 262–263 × 185 px; tensor entries per image 10 × 6 × 4 × 1 = 240 (R = 1) and 960 (R = 4).

***Calibration and analysis configuration***. The figure of Liu et al. (2019) was available as a 1900 × 1691 px JPEG raster at 300 ppi, from which the nine panels (622 × 466 px; 621 × 466 px in the middle column) were cropped. Each panel contains a 100-µm scale bar; the eight bars that could be measured automatically were 55–59 px long (median 58 px), which gives a pixel size of 1.72 µm and a field of about 1.07 × 0.80 mm, consistent with the 1.10 × 0.76 mm stated in the original caption. The pixel size of 4.5 µm given in the methods of the source article is not compatible with its own field size and was not used. Luminance was computed as Y = 0.299 R + 0.587 G + 0.114 B and z-scored over the whole panel. ROI = 1 is the central region left after removing a 48-px margin, which also removes the scale bar; ROI = 4 is its partition into four equal quadrants (Figure 1, Table 2). Derivative filters were applied to the whole panel with reflection at the borders and aggregated over each ROI; for the co-occurrence and autocorrelation channels, the partner pixel of each pair was taken from the reflected panel when the offset left the panel.

Besides the four reference scales s = 1, 2, 4 and 8 px (1.7–13.8 µm), two coarser scales, s = 16 and 32 px (27.6 and 55.2 µm), were added because the aggregates and macropores in the test images measure tens to hundreds of micrometres, so the tensor of each image had 10 × 6 × 4 entries per ROI. The anisotropy index A and texture axis ψ were obtained from the $D_2$ entries through the quadratic form of Proposition 1; ψ is given in degrees counter-clockwise from the image rows (+x), with y pointing upward, and is the direction of the dominant phase boundaries. Uncertainty was estimated by a block bootstrap in which each ROI was divided into an 8 × 8 grid of blocks (about 66 × 46 px for ROI = 1), which were resampled with replacement 1000 times (Künsch, 1989); 95 % confidence intervals (CI) are the 2.5th and 97.5th percentiles. The reference for isotropy was the 95th percentile of A over 200 isotropic surrogates with the radially averaged Fourier amplitude of each image and random phases (Theiler et al., 1992); the phases were taken from the Fourier transform of real Gaussian white noise, so that the surrogates are real-valued, and P = (1 + n≥)/(1 + N), where n≥ is the number of the N = 200 surrogates whose A is at least the observed value, so that the smallest attainable P is 1/201 = 0.005. The four quadrants differ in area by less than 0.4 %, so Proposition 2 applies with equal weights to within this tolerance. Spearman P values were obtained with the t approximation; for n = 8 exact permutation P values are larger for the strongest correlations (for example 0.011 instead of 0.007 for ρ = 0.86), and none of the P values is corrected for multiple comparisons.

The complementary representations followed the earlier muscle study (Ţălu, 2027a): the structure-tensor field at derivative scale 2 px with a Gaussian integration window of 10 px, from which the mean coherence κ and the resultant length R of the

energy- and coherence-weighted local axes were computed; the correlation length ξ(θ), defined as the lag at which the two-dimensional autocorrelation of $G_1$ over the ROI falls to 1/e along θ; and the characteristic scale s*, the maximum of the scale-normalized energy $s^2 \cdot \mathrm{tr}\, J$ evaluated at 19 log-spaced scales between 1 and 48 px and refined by a parabola in log s, together with its half-maximum band. Channel redundancy was measured by Spearman correlation over all entries of the R = 4 tensors at s = 1–8 px (Spearman, 1904). Tensors were compared through the normalized Euclidean distance between the 32 R = 4 tensors of the eight retained images (160 entries at s = 1–8 px, each standardized across ROIs, divided by √160) and average-linkage clustering.

***Exclusion and reference data***. Image f (OPP, 10–20 cm) was flagged before the analysis because a single section of decomposing plant residue occupies most of the field. Its results are reported for completeness, but it was excluded from comparisons, correlations and clustering, so that eight images were retained. Image i is also crossed by a residue channel, but the channel occupies a smaller fraction of the field and the image was retained. As independent references, the mean equivalent pore diameter D and pore-wall roughness reported by Liu et al. (2019) for each pattern and depth (their Table 2), and the bulk density, organic matter and proportion of water-stable aggregates > 0.25 mm (their Table 1), were related to the tensor readouts by Spearman correlation (n = 8). These references are plot-level values obtained from many fields per thin section, not from the specific fields analysed here, and they co-vary with depth, so the correlations are descriptive.

***Implementation and verification***. The tensor was implemented in Python (NumPy, SciPy, Matplotlib) following the reference definitions. Before the soil analysis, the implementation was run on the two muscle images of that study and reproduced its published values to the reported precision: the anisotropy indices and axes at four scales, the eight regional values, the means and modulation indices of the ten channels, the correlation lengths and the characteristic scales. Robustness to the ROI definition was checked by repeating the R = 1 analysis with margins of 32 and 64 px.

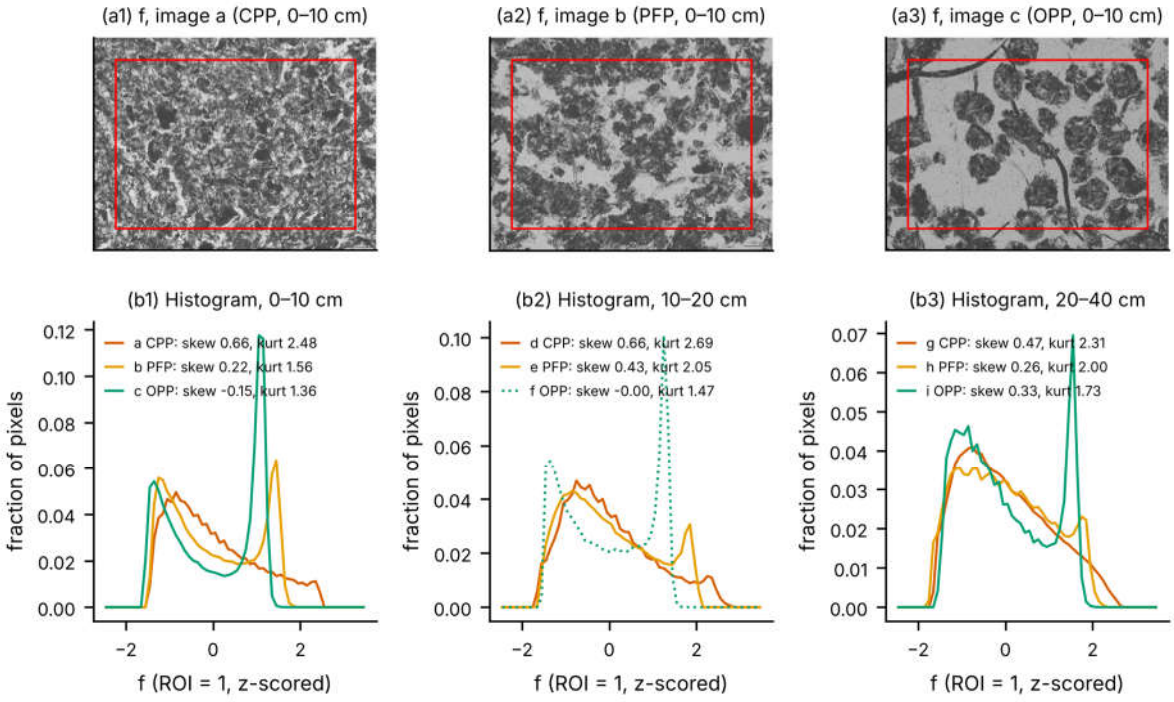


Figure 2. Luminance used for the tensor. (a1–a3) Z-scored luminance f of the three surface images (0–10 cm), with ROI = 1 (red). (b1–b3) Histogram of f within ROI = 1 for the three patterns at each depth, with skewness and kurtosis. The right-hand peak corresponds to resin-filled pores; image f (dotted) is excluded.

## Results

***Intensity distribution***. The luminance of all images was bimodal or skewed, with a dark solid phase and a bright, narrow peak of resin-filled pores (Figure 2). The pore peak was largest in the organic surface soil (image c), whose distribution was nearly symmetric and strongly platykurtic (skewness −0.15, kurtosis 1.36), whereas the conventional soils had a single broad mode with a bright tail (skewness 0.47–0.66, kurtosis 2.31–2.69) (Table 2). The tensor is computed on z-scored luminance, so these differences in phase proportions are retained in the shape channels but not in the overall level of the energy channels.

***Anisotropy across scales***. Figure 3 and Table 3 give A for ROI = 1 against scale. At the finest scales the micrographs were nearly isotropic. In the surface layer the $D_2$ shares at s = 2 px (3.4 µm) were 0.241–0.260 for all four orientations, and A was 0.037, 0.034 and 0.053 for CPP, PFP and OPP, with confidence intervals that reached down to the surrogate floor (0.017–0.021). Anisotropy was higher in the deeper layers: at s = 2 px, A was 0.073 (d) and 0.075 (e) at 10–20 cm, and 0.109 (g), 0.090 (h) and 0.214 (i) at 20–40 cm, all with lower CI bounds above the floor. Anisotropy generally increased with scale, but the surrogate floor rose faster (from 0.008–0.010 at s = 1 px to 0.16–0.19 at s = 32 px), because a larger operator leaves fewer independent texture elements in the ROI. At s = 16 px (27.6 µm), the scale of the aggregates, the organic surface soil was the only image with A below its floor (c: 0.066, floor 0.106). The conventional surface soil remained clearly anisotropic (a: 0.207, CI 0.108–0.326, floor 0.093), and the strongest coarse-scale anisotropy occurred in the soils crossed by planar voids or channels (d: 0.318; h: 0.278; i: 0.409).

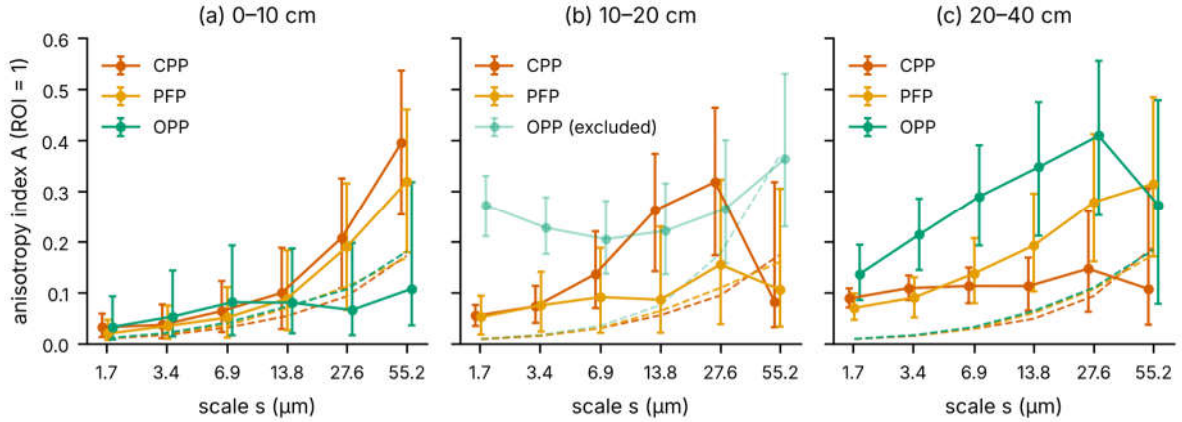


Figure 3. Anisotropy index A (ROI = 1) against scale s, with 95 % bootstrap CI (bars) and the 95th percentile of A over 200 isotropic surrogates (dashed, same colour). (a) 0–10 cm; (b) 10–20 cm; (c) 20–40 cm. Points are slightly offset horizontally for legibility. Image f (pale) is excluded.

Table 3

R = 1 tensor: anisotropy index A with 95 % bootstrap CI, 95th percentile of A for isotropic surrogates (null) and texture axis ψ (°, from +x, y upward) with 95 % CI, at s = 2 px (3.4 µm) and s = 16 px (27.6 µm)

| *Image (depth, cm)* | *A, s = 2 [95 % CI]* | *Null* | *ψ, s = 2 [95 % CI]* | *A, s = 16 [95 % CI]* | *Null* | *ψ, s = 16 [95 % CI]* |
|---|---|---|---|---|---|---|
| a – CPP, 0–10 | 0.037 [0.011, 0.076] | 0.017 | 97.8 [61.3, 132.9] | 0.207 [0.108, 0.326] | 0.093 | 112.1 [94.4, 124.7] |
| b – PFP, 0–10 | 0.034 [0.009, 0.074] | 0.020 | 2.1 [-38.5, 42.5] | 0.190 [0.066, 0.315] | 0.112 | 169.3 [152.3, 188.3] |
| c – OPP, 0–10 | 0.053 [0.014, 0.143] | 0.021 | 108.8 [41.8, 178.4] | 0.066 [0.017, 0.197] | 0.106 | 108.3 [41.9, 182.5] |
| d – CPP, 10–20 | 0.073 [0.040, 0.113] | 0.015 | 92.8 [81.4, 106.5] | 0.318 [0.173, 0.465] | 0.094 | 97.9 [86.3, 111.8] |
| e – PFP, 10–20 | 0.075 [0.023, 0.141] | 0.016 | 154.5 [128.1, 178.6] | 0.155 [0.038, 0.323] | 0.109 | 131.2 [91.8, 178.4] |
| f* – OPP, 10–20 | 0.227 [0.176, 0.287] | 0.017 | 52.1 [46.3, 57.5] | 0.265 [0.158, 0.400] | 0.176 | 36.9 [18.5, 55.3] |
| g – CPP, 20–40 | 0.109 [0.085, 0.134] | 0.015 | 3.3 [-4.2, 10.1] | 0.147 [0.062, 0.260] | 0.093 | 165.2 [146.0, 189.0] |
| h – PFP, 20–40 | 0.090 [0.051, 0.130] | 0.016 | 35.9 [21.6, 48.9] | 0.278 [0.161, 0.413] | 0.106 | 47.1 [32.7, 63.4] |
| i – OPP, 20–40 | 0.214 [0.144, 0.285] | 0.016 | 22.3 [16.2, 28.2] | 0.409 [0.253, 0.556] | 0.109 | 18.4 [7.0, 25.0] |

* Image f excluded from comparisons (single plant residue occupying most of the field). CIs of ψ may extend beyond 0–180° because the axis is a circular quantity.

***Orientation and regional heterogeneity***. Where the micrographs contain elongated pores, the texture axis followed them (Figures 4 and 5). In image d (CPP, 10–20 cm), which is crossed by near-vertical planar voids, ψ was 92.8° (CI 81.4–106.5°) at s = 2 px and stayed between 93° and 98° up to s = 16 px. In image h (PFP, 20–40 cm), with a diagonal planar void from lower left to upper right, ψ was 35.9° (21.6–48.9°) and turned towards the void (41–47°) at s = 8–16 px. In image i (OPP, 20–40 cm), with a channel formed around a decomposing residue, ψ was 22.3° (16.2–28.2°) and remained within 18–26° at all scales. Image g (CPP, 20–40 cm, dense angular blocky) had a weak horizontal axis (3.3°, CI −4.2 to 10.1°). This is compatible with the weakly separated plates described for the conventional soil (Liu et al., 2019), but the micrograph shows no distinct planar void. In the surface soils, the axis was poorly determined (CI widths of 70–137°), as expected when A is close to the floor. The structure-tensor field shows the same contrast locally (Figure 5): the resultant length of the local axes was 0.12–0.16 in the surface images and 0.31–0.54 in images d, g, h and i. The mean coherence was highest in the organic soils (c: 0.39; i: 0.36), whose aggregate outlines are smooth and locally coherent, although they share no common direction.

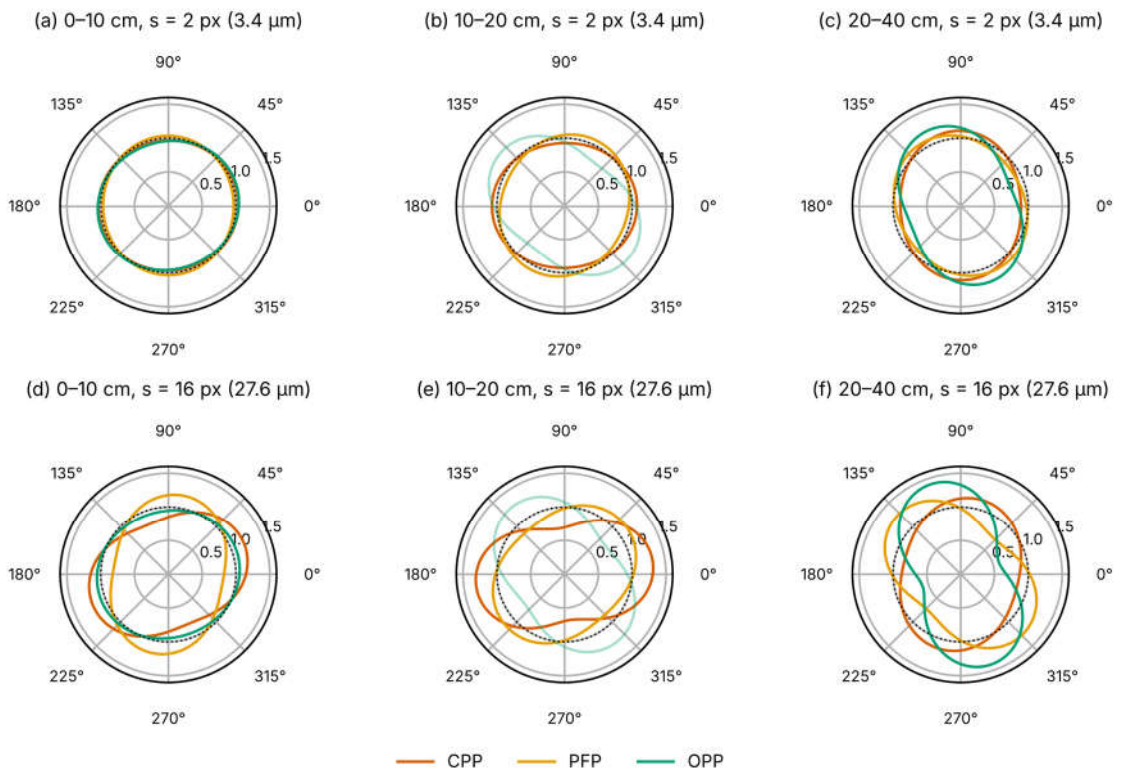


Figure 4. Directional profiles of the R = 1 tensor, $D_2(\theta)$ divided by its mean over θ, reconstructed from the four tensor entries through the quadratic form (Proposition 1), at s = 2 px (a–c) and s = 16 px (d–f) for the three patterns at each depth. Dotted circle: no directional preference. The profile is elongated perpendicular to the texture axis. Image f (pale) is excluded.

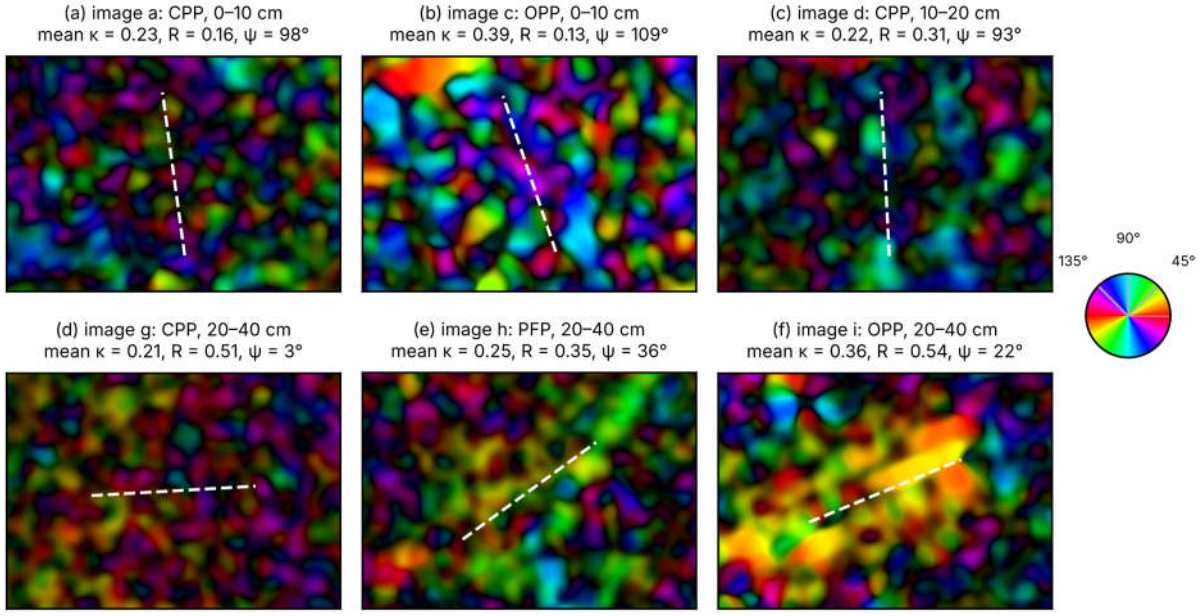


Figure 5. Structure-tensor field of ROI = 1 (derivative scale 2 px, integration window 10 px) for six images. Hue: local texture axis (colour wheel); brightness: coherence κ. Dashed line: texture axis ψ of the tensor at s = 2 px. Mean κ and resultant length R of the weighted local axes are given above each panel.

Table 4

R = 4 tensor at s = 2 px: anisotropy index A and texture axis ψ of each quadrant, range of the surrogate 95th percentiles, pooled A (R = 1) against the energy-weighted mean of the four regional values (right-hand side of Eq. 6), and the resulting pooling loss

| Image (depth, cm) | ROI 1 | ROI 2 | ROI 3 | ROI 4 | Null | Pooled / weighted mean | Loss (%) |
|---|---|---|---|---|---|---|---|
| a – CPP, 0–10 | 0.072 (156°) | 0.046 (82°) | 0.112 (105°) | 0.068 (62°) | 0.050–0.054 | 0.037 / 0.075 | 51 |
| b – PFP, 0–10 | 0.079 (150°) | 0.061 (73°) | 0.069 (176°) | 0.102 (16°) | 0.055–0.058 | 0.034 / 0.078 | 56 |
| c – OPP, 0–10 | 0.025 (171°) | 0.028 (118°) | 0.087 (77°) | 0.149 (113°) | 0.055–0.065 | 0.053 / 0.073 | 28 |
| d – CPP, 10–20 | 0.037 (95°) | 0.079 (98°) | 0.070 (76°) | 0.118 (97°) | 0.047–0.050 | 0.073 / 0.076 | 4 |
| e – PFP, 10–20 | 0.048 (36°) | 0.145 (142°) | 0.155 (154°) | 0.049 (168°) | 0.045–0.049 | 0.075 / 0.098 | 23 |
| f* – OPP, 10–20 | 0.236 (52°) | 0.372 (50°) | 0.151 (48°) | 0.170 (59°) | 0.048–0.054 | 0.227 / 0.230 | 1 |
| g – CPP, 20–40 | 0.123 (24°) | 0.095 (157°) | 0.200 (11°) | 0.104 (165°) | 0.047–0.051 | 0.109 / 0.132 | 18 |
| h – PFP, 20–40 | 0.105 (3°) | 0.185 (49°) | 0.155 (25°) | 0.075 (76°) | 0.045–0.049 | 0.090 / 0.129 | 30 |
| i – OPP, 20–40 | 0.153 (28°) | 0.206 (11°) | 0.372 (24°) | 0.122 (28°) | 0.050–0.054 | 0.214 / 0.220 | 3 |

* Image f excluded from comparisons.

The four-ROI tensor shows how the surface soils lose their directional signal when pooled (Table 4). In images a and b the quadrants had A = 0.046–0.112 and 0.061–0.102, but their axes were spread over the half-circle, so the pooled A (0.037 and 0.034) was only about half of the energy-weighted mean of the regional values (pooling losses of 51 % and 56 %). This is the attenuation predicted by Proposition 2. Where a single feature dominated, the quadrant axes agreed and the loss was small (d: 4 %; i: 3 %; f: 1 %). The surrogate floors of the quadrants (0.045–0.065) were about three times those of ROI = 1, so only the larger regional values were resolved.

***Characteristic scale and spatial correlation***. The scale readouts ordered the management systems in the same way wherever they could be compared: all three systems at 0–10 and 20–40 cm, and CPP and PFP at 10–20 cm, where the OPP image was excluded (Figures 6 and 7, Table 5). The scale-normalized energy of the conventional soils peaked at s* = 2.4–3.8 μm and fell off steeply, whereas that of the organic surface soil peaked at 18.7 μm with a half-maximum band extending to 54 μm (Figure 6a–c). Correlation lengths were nearly independent of direction and ranked CPP < PFP < OPP at 0–10 and 20–40 cm and CPP < PFP at 10–20 cm: 10.9, 25.5 and 31.3 μm at 0–10 cm; 10.2 and 14.3 μm (CPP, PFP) at 10–20 cm; and 9.0, 13.5 and 26.3 μm at 20–40 cm. The quadrant values (Figure 7a,b) show that this ordering was not produced by a single region. The quadrant ranges of the conventional soils (7.9–12.9 μm) did not overlap those of the organic surface soil (21.0–38.8 μm). The pollution-free and organic soils at 20–40 cm overlapped partly (8.9–18.9 and 12.8–29.8 μm). Among the channels at s = 2 px, the gradient kurtosis $D_3$ (CPP 3.25–3.72; PFP 3.57–4.26; OPP 4.56–5.69) and the autocorrelation $D_{10}$ at lag 2s (CPP 0.69–0.74; PFP 0.78–0.88; OPP 0.87–0.91) followed the same order (Figure 7c,d). The gradient energy $D_2$ of the z-scored image was highest in the conventional soils at 0–10 and 20–40 cm (0.0195 and 0.0210, against 0.0107 and 0.0141 in OPP) and practically equal in CPP and PFP at 10–20 cm (0.0185 and 0.0188). Had image f been retained, its values (ξ = 150 μm, s* at the upper limit of the examined range, $D_3$ = 5.76, $D_{10}$ = 0.940) would have continued the same order at 10–20 cm, but they are dominated by the residue and are not used as evidence. These values describe a fine-grained, densely packed matrix in which variance is lost at a few micrometres, against a soil of larger aggregates separated by wide pores, in which strong edges are sparse and intensity remains correlated over tens of micrometres.

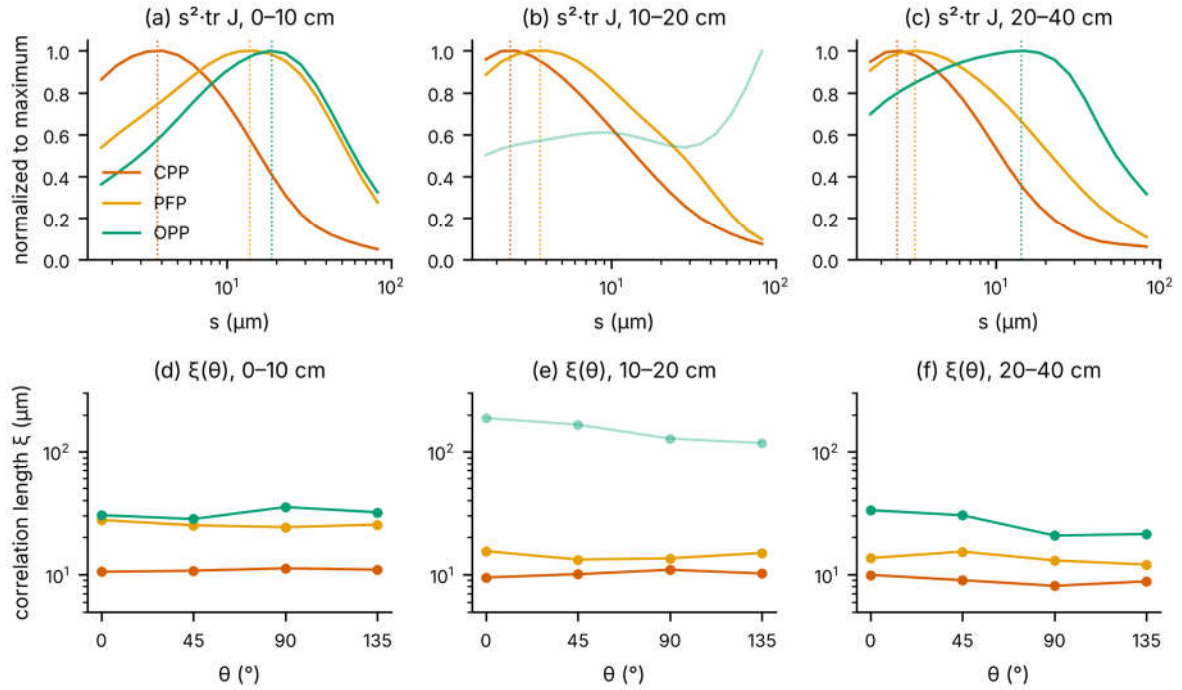


Figure 6. Scale and spatial correlation of ROI = 1. (a–c) Scale-normalized derivative energy $s^2 \cdot tr\, J$ (variance-loss rate, Eq. 7) against s, normalized to its maximum; dotted lines: characteristic scale s*. (d–f) Correlation length ξ(θ) at the four configured orientations (logarithmic ordinate). Image f (pale) is excluded; its s* lies at the upper end of the examined range.

Table 5

Scale and spatial-correlation readouts (R = 1; ranges over the four quadrants of R = 4 in parentheses): mean correlation length ξ over the four orientations, characteristic scale s* and half-maximum band of $s^2 \cdot tr\, J$, channel means over θ at s = 2 px of the gradient energy $D_2$, the gradient kurtosis $D_3$ and the autocorrelation $D_{10}$, and the mean coherence κ / resultant length R of the structure-tensor field. Lengths in µm

| *Image (depth, cm)* | *ξ (quadrants)* | *s* (quadrants)* | *Half-max band* | *$D_2$* | *$D_3$* | *$D_{10}$* | *κ / R* |
|---|---|---|---|---|---|---|---|
| a – CPP, 0–10 | 10.9 (10.0–12.0) | 3.8 (3.4–4.3) | 1.7–14.8 | 0.0195 | 3.58 | 0.739 | 0.23 / 0.16 |
| b – PFP, 0–10 | 25.5 (20.8–28.3) | 13.7 (10.1–20.0) | 1.7–53.8 | 0.0127 | 4.26 | 0.879 | 0.26 / 0.12 |
| c – OPP, 0–10 | 31.3 (21.0–38.8) | 18.7 (13.9–34.1) | 3.3–53.8 | 0.0107 | 5.69 | 0.905 | 0.39 / 0.13 |
| d – CPP, 10–20 | 10.2 (7.9–12.9) | 2.4 (2.1–3.1) | 1.7–11.9 | 0.0185 | 3.72 | 0.730 | 0.22 / 0.31 |
| e – PFP, 10–20 | 14.3 (11.1–17.7) | 3.7 (2.7–7.0) | 1.7–22.8 | 0.0188 | 3.84 | 0.792 | 0.29 / 0.24 |
| f* – OPP, 10–20 | 150.0 (14.2–65.6) | 82.8† (4.1–82.8) | 1.7–82.8 | 0.0075 | 5.76 | 0.940 | 0.34 / 0.62 |
| g – CPP, 20–40 | 9.0 (8.6–9.1) | 2.5 (2.4–2.6) | 1.7–9.6 | 0.0210 | 3.25 | 0.689 | 0.21 / 0.51 |
| h – PFP, 20–40 | 13.5 (8.9–18.9) | 3.2 (2.7–3.8) | 1.7–18.4 | 0.0186 | 3.57 | 0.781 | 0.25 / 0.35 |
| i – OPP, 20–40 | 26.3 (12.8–29.8) | 14.3 (2.9–19.3) | 1.7–53.8 | 0.0141 | 4.56 | 0.869 | 0.36 / 0.54 |

* Image f excluded from comparisons. † Maximum at the upper end of the examined scale range. A lower band limit of 1.7 µm means that the band extends below the smallest scale examined.

***Channel redundancy***. Over the 512 entries of the eight R = 4 tensors at s = 1–8 px, the gradient channels were again practically collinear (Spearman $\rho(D_1,D_2) = 1.00$, $\rho(D_1,D_5) = 0.99$, $\rho(D_2,D_5) = 0.99$), as in guppy and porcine muscle (Ţălu, 2026b, 2027b). The gradient entropy $D_4$ was nearly independent of them ($\rho = -0.06$ to $-0.12$) and strongly anticorrelated with the kurtosis $D_3$ ($\rho = -0.83$). Among the co-occurrence channels, contrast and homogeneity were closely linked ($\rho(D_6,D_7) = -0.92$), but contrast was only moderately related to energy and correlation ($\rho = -0.62$ and $-0.58$), and correlation $D_9$ was associated with the autocorrelation $D_{10}$ ($\rho = 0.80$). The directional modulation of GLCM contrast at s = 2 px was 0.30–0.40 in every image, close to the grid-induced value of 0.30 found for isotropic reference fields (Ţălu, 2027a), so it cannot be read as soil anisotropy.

***Agreement with independent micromorphometric and physical data***. Across the eight retained images, the scale readouts were correlated with the pore measurements reported for the same plots (Figure 7e, Table 6). The mean correlation length increased with the mean equivalent pore diameter (ρ = 0.86, P = 0.007) and with pore-wall roughness (ρ = 0.95). The characteristic scale, the kurtosis $D_3$ and the autocorrelation $D_{10}$ behaved similarly (ρ = 0.81–0.90 with pore diameter), and the gradient energy $D_2$ was negatively correlated (ρ = −0.74). By contrast, the fine-scale anisotropy A at s = 2 px was correlated with bulk density (ρ = 0.80, P = 0.017) and negatively with organic matter (ρ = −0.83) and aggregate stability (ρ = −0.76), but not with pore diameter (ρ = −0.52, P = 0.18) (Figure 7f). Both bulk density and anisotropy increase with depth in this soil, and the most anisotropic image (i) owes its value to a single channel, so the association between A and bulk density reflects depth as much as management.

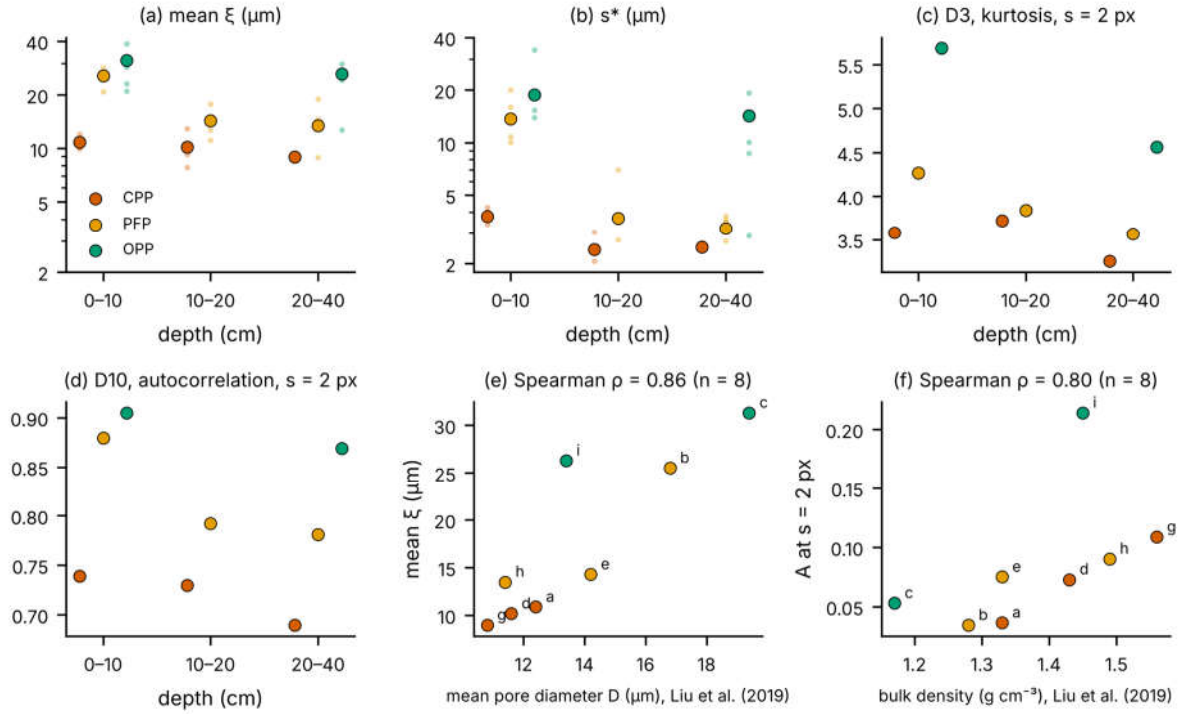


Figure 7. Summary of the readouts that separate the management systems. (a) Mean correlation length ξ and (b) characteristic scale s* for ROI = 1 (large symbols) and the four quadrants of R = 4 (small symbols); (c) gradient kurtosis $D_3$ and (d) autocorrelation $D_{10}$ at s = 2 px. (e) Mean ξ against the mean equivalent pore diameter and (f) A at s = 2 px against bulk density reported for the same plots by Liu et al. (2019); letters identify the images. n = 8 (image f excluded).

Table 6

Spearman correlation (P in parentheses) between tensor readouts of ROI = 1 and plot-level soil properties reported by Liu et al. (2019) for the same pattern and depth (n = 8 images; image f excluded). ξ and s* in µm; channel means at s = 2 px

| *Soil property* | *ξ* | *s** | *$D_2$* | *$D_3$* | *$D_{10}$* | *A (s = 2)* |
|---|---|---|---|---|---|---|
| Mean equivalent pore diameter D | 0.86 (0.007) | 0.81 (0.015) | -0.74 (0.037) | 0.90 (0.002) | 0.90 (0.002) | -0.52 (0.183) |
| Pore-wall roughness R | 0.95 (< 0.001) | 0.93 (0.001) | -0.79 (0.021) | 0.90 (0.002) | 0.98 (< 0.001) | -0.40 (0.320) |
| Bulk density | -0.62 (0.099) | -0.63 (0.091) | 0.61 (0.108) | -0.72 (0.045) | -0.72 (0.045) | 0.80 (0.017) |
| Soil organic matter | 0.60 (0.120) | 0.64 (0.086) | -0.60 (0.120) | 0.69 (0.058) | 0.69 (0.058) | -0.83 (0.010) |
| Water-stable aggregates > 0.25 mm | 0.64 (0.086) | 0.62 (0.102) | -0.62 (0.102) | 0.74 (0.037) | 0.74 (0.037) | -0.76 (0.028) |

The reference values are means over many fields of each thin section, not values of the analysed fields, and they co-vary with depth; P values (t approximation) are descriptive and uncorrected for multiple comparisons.

***Distance between regional tensors***. Figure 8 shows the normalized distance between the 32 regional tensors. The mean distance was 0.82 between quadrants of the same

image, 1.09 between quadrants of different images under the same management and 1.43 between images under different management. Apart from quadrant c3, which is almost entirely resin and forms a cluster of its own, average-linkage clustering separated two groups: the quadrants of images a, d, e, g and h, and those of b, c and i. This partition coincides with the microstructure described by the original authors better than with management. The first group contains the blocky and angular-blocky microstructures of all CPP images and of the deeper PFP images. The second contains the crumb microstructures of the PFP and OPP surface soils, together with the channel-bearing OPP subsoil (Table 2).

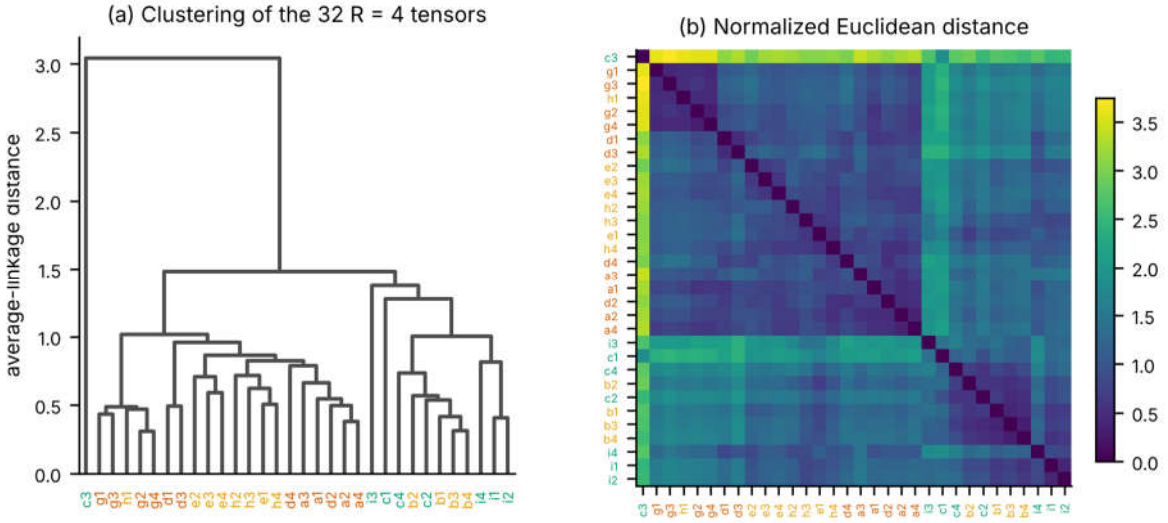


Figure 8. (a) Average-linkage clustering and (b) normalized Euclidean distance between the 32 R = 4 tensors (160 entries at s = 1–8 px, each standardized across the 32 ROIs) of the eight retained images; labels give the image and quadrant, coloured by planting pattern (CPP, orange-red; PFP, amber; OPP, green).

***Sensitivity to the ROI***. Changing the margin of ROI = 1 from 48 px to 32 or 64 px changed the mean correlation length and the characteristic scale of every retained image by at most 7 %, and preserved their ordering. The fine-scale anisotropy was more sensitive in weakly anisotropic images: A at s = 2 px of image c varied between 0.037 and 0.082. In image g it was stable (0.109–0.112).

**Discussion**. The nine micrographs support four statements within the limits stated below. First, the readouts that distinguished the soils under different management were the scale and spatial-correlation readouts: the characteristic scale, the correlation length, the kurtosis of the directional derivatives and the autocorrelation at a lag of twice the scale. They ranked the conventional, pollution-free and organic soils in the same order at 0–10 and 20–40 cm, and the conventional below the pollution-free soil at 10–20 cm, where the organic image was excluded. This is the order of porosity, organic matter and aggregate stability measured in the same plots (Liu et al., 2019). Across images, the correlation length followed the mean pore diameter reported for the same plots. In a two-phase image, the correlation length is expected to reflect the typical size of the solid and pore domains, and the variance-loss maximum s* marks the width of the dominant intensity transitions (Eq. 7). Both are therefore segmentation-free summaries related to the sizes of aggregates and pores in the analysed images; they are not direct measurements of pore size or porosity. The conventional soils lost most of their variance at 2–4 μm, the scale of a dense matrix of fine particles and simple packing voids. The organic surface soil lost it at about 19 μm and over a band reaching 50 μm, the scale of well-separated crumbs.

Second, unlike the muscle sections of the earlier study, where fibre boundaries gave A = 0.21–0.39 at s = 2 px (Ţălu, 2027a), soil thin sections at 3.4 μm were nearly

isotropic, especially in the surface layer. Anisotropy appeared where the soil contains oriented voids. The texture axis then pointed along the visible planar voids, cracks and channels (images d, h and i) without any segmentation, which is the soil counterpart of the agreement between tensor axis and fibre orientation found in guppy muscle (Ţălu, 2026b). Fine-scale anisotropy increased with depth and bulk density. This is consistent with the denser, more platy and fissured fabric of compacted subsoils (Pagliai et al., 2004; Hamza & Anderson, 2005), but in the present data depth and management cannot be separated, and one high value comes from a residue channel. At the aggregate scale, the rounded crumbs of the organic surface soil were the only texture whose anisotropy did not exceed the isotropic floor, whereas the blocky conventional surface soil remained anisotropic. In these images, scale-resolved anisotropy therefore helped to distinguish crumb from blocky microstructure, provided the surrogate floor, which rises steeply with scale, is reported with each value.

Third, regional heterogeneity matters more in soils than in the muscle sections. The pooling inequality of Proposition 2 explained why the surface soils appeared isotropic as a whole although their quadrants were individually anisotropic: the regional axes disagreed, and pooling removed about half of the directional signal (51–56 %). A single anisotropy value for a whole thin-section field is therefore an adequate summary only when one feature dominates it. The four-ROI tensor shows whether this is the case. Fourth, channel redundancy behaved as in the muscle sections: $D_1$, $D_2$ and $D_5$ were practically collinear, and GLCM contrast carried a grid-induced directional modulation of about 0.30. In soil, the kurtosis $D_3$ and the autocorrelation $D_{10}$ were among the most informative channels, because they respond to the two-phase, edge-sparse character of well-aggregated soil. The distance analysis grouped the regional tensors by microstructure type (crumb versus blocky) rather than by management. This suggests that the tensor responds to the morphological categories used by micromorphologists (Stoops, 2021), and that management effects enter through the microstructure they produce.

From the viewpoint of soil-health assessment, these results suggest a compact set of candidate image-based indicators that need no thresholding: a characteristic scale and a correlation length in micrometres for the size of the structural units, and an anisotropy index with its scale, surrogate floor and texture axis for oriented voids. Such indicators could complement porosity measurements from binarized images (Pagliai et al., 2004; Ringrose-Voase, 1991) and the qualitative description of microstructure (Stoops, 2021; Verrecchia & Trombino, 2021). Because they are computed on the same tensor, they remain linked to an explicit scale, direction and region, as required for reproducible texture measurement (Zwanenburg et al., 2020).

**Limitations**. Each pattern–depth combination was represented by a single published field, chosen by the original authors as representative, and the plot-level reference data come from other fields of the same sections; therefore no statistical inference about management was attempted, and the correlations with soil properties are descriptive and confounded with depth. The images are JPEG-compressed panels of a published figure, with a calibration derived from the printed scale bars and a resolution (1.72 µm) coarser than that of the original acquisitions; compression may affect the finest scale. Only plane-polarized light was used, so transparent mineral grains have the same luminance as pores, a known source of overestimation of porosity that the original authors corrected with cross-polarized images. The isotropic surrogates are Gaussian and do not reproduce the bimodal intensity distribution of thin sections; their P values (resolution 0.005) indicate departure from an isotropic spectrum, not agronomic significance. The block bootstrap treats blocks as exchangeable, and at s = 16–32 px the blocks (about 66 × 46 px) are comparable to or smaller than the support of the Gaussian operators, so the coarse-scale intervals are approximate. Finally, two-dimensional sections cannot describe pore connectivity, which requires three-dimensional imaging (Rabot et al., 2018). The next steps are an analysis of complete mosaics of several thin sections per plot with replicate plots, a comparison with segmentation-based porosity and with single-scale texture baselines (Ojala et al., 2002), and an extension to X-ray tomography slices.

**Conclusions**. A hierarchical descriptor tensor indexed by channel, scale, orientation and region was applied to published thin-section micrographs of a greenhouse soil after ten years of conventional, pollution-free and organic management. The implementation was first verified against the published values of the earlier muscle study. In the soil images, the characteristic scale, the correlation length, the gradient kurtosis and the autocorrelation ranked the management systems consistently wherever they could be compared, that is, all three systems at 0–10 and 20–40 cm and two at 10–20 cm (correlation length at 0–10 cm: 10.9, 25.5 and 31.3 μm). Across images, the correlation length agreed with the mean pore diameter measured in the same plots ($\rho = 0.86$). Anisotropy was weak at fine scale, increased with depth and bulk density, and its texture axis pointed along the visible planar voids, cracks and channels. At the aggregate scale, the anisotropy of the crumb microstructure of the organic surface soil did not exceed the isotropic floor. The pooling inequality quantified a loss of about half of the directional signal in the heterogeneous surface soils, and the regional tensors grouped by microstructure type. The tensor therefore provides segmentation-free, physically scaled and internally consistent readings of soil structure in the analysed images. Establishing their value as indicators of soil health requires replicated, calibrated thin-section mosaics.

**Acknowledgement.** The author thanks the authors of Liu et al. (2019) for publishing their thin-section micrographs under an open licence.

**Authors Contributions**. Ştefan Ţălu contributed to all aspects of the work.

**Conflicts of Interest**. The author declares that there is no conflict of interest.

**Copyright and Permissions**. The micrographs in Figure 1, and the images from which Figures 2 and 5 were computed, are reproduced from an open-access article published by Springer Nature in *Scientific Reports* under the Creative Commons Attribution 4.0 International licence (CC BY 4.0) (Liu et al., 2019), which permits reuse and adaptation with appropriate citation and indication of changes; the source, licence and changes are stated in the caption. All other figures were produced by the author.

**Data Availability**. The analysis code, ROI coordinates, the complete numerical results (including those of the excluded image f) and the processing parameters are available from the corresponding author upon request.

**Use of generative AI**. During the preparation of this manuscript, the author used GPT-6 Astra to assist in the preparation of the graphical abstract and a figure. The author reviewed and edited the AI-assisted visual materials as necessary and takes full responsibility for the accuracy, originality, and integrity of all content in the manuscript.

**Funding**. This research received no external funding.

## References

Bigün, J., & Granlund, G. H. (1987). Optimal orientation detection of linear symmetry. In *Proceedings of the First International Conference on Computer Vision* (pp. 433–438). London.

Bronick, C. J., & Lal, R. (2005). Soil structure and management: A review. *Geoderma, 124*(1–2), 3–22. https://doi.org/10.1016/j.geoderma.2004.03.005

Depeursinge, A. (2017). Multiscale and multidirectional biomedical texture analysis: Finding the needle in the haystack. In A. Depeursinge, O. S. Al-Kadi, & J. R. Mitchell (Eds.), *Biomedical Texture Analysis* (pp. 29–53). Academic Press.

Freeman, W. T., & Adelson, E. H. (1991). The design and use of steerable filters. *IEEE Transactions on Pattern Analysis and Machine Intelligence, 13*(9), 891–906. https://doi.org/10.1109/34.93808

Hamza, M. A., & Anderson, W. K. (2005). Soil compaction in cropping systems: A review of the nature, causes and possible solutions. *Soil and Tillage Research, 82*(2), 121–145. https://doi.org/10.1016/j.still.2004.08.009

Haralick, R. M., Shanmugam, K., & Dinstein, I. (1973). Textural features for image classification. *IEEE Transactions on Systems, Man, and Cybernetics, SMC-3*(6), 610–621. https://doi.org/10.1109/TSMC.1973.4309314

Künsch, H. R. (1989). The jackknife and the bootstrap for general stationary observations. *The Annals of Statistics, 17*(3), 1217–1241. https://doi.org/10.1214/aos/1176347265

Lindeberg, T. (1998). Feature detection with automatic scale selection. *International Journal of Computer Vision, 30*(2), 79–116. https://doi.org/10.1023/A:1008045108935

Liu, Z., Han, J., Sun, Z., Chen, T., Hou, Y., Lei, N., Dong, Q., He, J., & Lu, Y. (2019). Long-term effects of different planting patterns on greenhouse soil micromorphological features in the North China Plain. *Scientific Reports, 9*, 2200. https://doi.org/10.1038/s41598-019-38499-6

Mardia, K. V., & Jupp, P. E. (2000). *Directional statistics*. John Wiley & Sons.

Ojala, T., Pietikäinen, M., & Mäenpää, T. (2002). Multiresolution gray-scale and rotation invariant texture classification with local binary patterns. *IEEE Transactions on Pattern Analysis and Machine Intelligence, 24*(7), 971–987. https://doi.org/10.1109/TPAMI.2002.1017623

Pagliai, M., Vignozzi, N., & Pellegrini, S. (2004). Soil structure and the effect of management practices. *Soil and Tillage Research, 79*(2), 131–143. https://doi.org/10.1016/j.still.2004.07.002

Perfect, E., & Kay, B. D. (1995). Applications of fractals in soil and tillage research: A review. *Soil and Tillage Research, 36*(1–2), 1–20. https://doi.org/10.1016/0167-1987(96)81397-3

Rabot, E., Wiesmeier, M., Schlüter, S., & Vogel, H.-J. (2018). Soil structure as an indicator of soil functions: A review. *Geoderma, 314*, 122–137. https://doi.org/10.1016/j.geoderma.2017.11.009

Ringrose-Voase, A. J. (1991). Micromorphology of soil structure: Description, quantification, application. *Australian Journal of Soil Research, 29*(6), 777–813. https://doi.org/10.1071/SR9910777

Spearman, C. (1904). The proof and measurement of association between two things. *American Journal of Psychology, 15*(1), 72–101. https://doi.org/10.2307/1412159

Stoops, G. (2021). *Guidelines for analysis and description of soil and regolith thin sections* (2nd ed.). Soil Science Society of America / John Wiley & Sons.

Ţălu, Ş. (2012). Texture analysis methods for the characterisation of biological and medical images. *Extreme Life, Biospeology & Astrobiology, 4*(1), 8–12.

Ţălu, Ş. (2015). *Micro and nanoscale characterization of three dimensional surfaces: Basics and applications*. Napoca Star Publishing House, Cluj-Napoca, Romania.

Ţălu, Ş. (2026a). A multidimensional implementation lattice for translational human and veterinary medicine. *Human & Veterinary Medicine, 18*(1), 9–23.

Ţălu, Ş. (2026b). Application of the hierarchical texture-descriptor tensor to histological muscle sections of *Poecilia reticulata*. *Poeciliid Research, 16*(1), 62-74. https://doi.org/10.67784/0096

Ţălu, Ş. (2027a). A hierarchical tensor framework for quantitative multiscale and multidirectional biomedical texture characterization. *Human & Veterinary Medicine, 19*(1), 32-53. https://doi.org/10.67784/0095

Ţălu, Ş. (2027b). Coherence, alignment and fibre-profile geometry in a hierarchical texture-descriptor tensor: Application to H&E sections of skeletal muscle in wild boar (*Sus scrofa*) and domestic pigs. *Porcine Research, 17*(1), 1–22. https://doi.org/10.67784/0098

Ţălu, Ş. (2027c). Descriptor-tensor texture analysis of myostatin-edited rabbit muscle: A two-study replication. *Rabbit Genetics, 17*(1), 10–24. https://doi.org/10.67784/0097.

Theiler, J., Eubank, S., Longtin, A., Galdrikian, B., & Farmer, J. D. (1992). Testing for nonlinearity in time series: The method of surrogate data. *Physica D, 58*(1–4), 77–94. https://doi.org/10.1016/0167-2789(92)90102-S

Traverso, A., Wee, L., Dekker, A., & Gillies, R. (2018). Repeatability and reproducibility of radiomic features: A systematic review. *International Journal of Radiation Oncology, Biology, Physics, 102*(4), 1143–1158. https://doi.org/10.1016/j.ijrobp.2018.05.053

Verrecchia, E. P., & Trombino, L. (2021). *A visual atlas for soil micromorphologists*. Springer. https://doi.org/10.1007/978-3-030-67806-7

Zwanenburg, A., Vallières, M., Abdalah, M. A., Aerts, H. J. W. L., Andrearczyk, V., Apte, A., Ashrafinia, S., Bakas, S., Beukinga, R. J., Boellaard, R., Bogowicz, M., et al. (2020). The Image Biomarker Standardization Initiative: Standardized quantitative radiomics for high-throughput image-based phenotyping. *Radiology, 295*(2), 328–338. https://doi.org/10.1148/radiol.2020191145

Received: 01 October 2026. Accepted: 31 October 2026. Published online: 31 October 2026.
Author:
Ştefan Ţălu, The Directorate of Research, Development and Innovation Management (DMCDI), The Technical University of Cluj-Napoca, Constantin Daicoviciu St., no. 15, Cluj-Napoca 400020, Cluj County, Romania, e-mail: stefan.talu@auto.utcluj.ro; stefan.talu1@gmail.com https://orcid.org/0000-0003-1311-7657
This is an open-access article distributed under the terms of the Creative Commons Attribution License (CC-BY 4.0), which permits unrestricted use, distribution and reproduction in any medium, provided the original author and source are credited.
How to cite this article:
Ţălu, Ş. (2027). Scale and orientation signatures of soil structure in thin sections: A hierarchical descriptor tensor applied to greenhouse soils under conventional, pollution-free and organic management. *Advances in Environmental Sciences, 19*(1), 53–70. https://doi.org/10.67784/0099